Aleni, Afshin Hasani; Ituarte, Iñigo Flores; Mohite, Ashish; St-Pierre, Luc; Partanen, Jouni

Comparing stiffness of solid and scaffold nano-TiO2 structures produced by material extrusion method

Published in:
Ceramics International

DOI:
10.1016/j.ceramint.2017.10.181

Published: 01/01/2018

Document Version
Peer-reviewed accepted author manuscript, also known as Final accepted manuscript or Post-print

Comparing stiffness of solid and scaffold nano-TiO_2 structures produced by material extrusion method

Afshin Hasani Aleni, Iñigo Flores Ituarte, Ashish Mohite, Luc St-Pierre, Jouni Partanen
Additive Manufacturing Group, Mechanical Engineering Department, Aalto University, Espoo, Finland

Abstract- This study corresponds to the first stage of a project that focuses on optimizing the mechanical properties of titanium dioxide (TiO_2) for use in bone implants. The goal of the study is to characterize and compare the stiffness of solid and scaffold TiO_2 samples fabricated via three-dimensional material extrusion method. The sample specimens were sintered in a furnace at three different temperatures, namely-1200 °C, 1250 and 1300 °C- for 4 h. The sintering procedure caused shrinkage in all dimensions and the maximum shrinkage (57.5%) was observed in the direction perpendicular to the work plate. The morphology of the sintered samples was analyzed via scanning electron microscopy. This revealed that increasing the sintering temperature increased the grain size and decreased porosity. For example, the porosity of the samples sintered at 1300 °C was 20% less than that of samples sintered at 1200 °C. Uniaxial compression tests showed that scaffold structures had a lower stiffness than their solid counterparts, and the decrease in stiffness was comparable to the reduction in cross-sectional area. The elastic modulus of TiO_2 produced here by material extrusion was between 2.08-5.90 GPa, which is close to the elastic modulus of high density cancellous bone at 0.8-1.5 GPa. This is an important advantage as minimizing the mismatch in stiffness between bone and implant is critical to avoid problems such as stress shielding and bone resorption.

Keywords: Titanium dioxide (TiO_2); 3D printing; Scaffold structure; Additive manufacturing; Ceramic

Introduction

Traditional metal implants, such as pure titanium and stainless steels, are widely used for fixing bone fractures and internal devices of bone parts because of their high mechanical strengths, biocompatibility, and bioactivity [1-3]. However, the high mechanical strengths of these implants also lead to problems after implantation. Stress shielding and bone resorption constitute problematic phenomena that occur in bone and implant metal-joint interfaces and especially around hip stems owing to the non-compliance of mechanical properties and flexibilities between intact bones and implant metals [4-5]. Huiskes et al. [6] and Fouad [7] proposed solutions for stress shielding and bone resorption. Huiskes et al. [6] scanned a proximal femur bone using a computed tomography (CT) scanner and analyzed a stem treated femur and intact femur using the finite element method. The results revealed that a reduction in the stem elastic modulus led to a significant decrease in long-term bone resorption, and the reduction in the stem stiffness led to a decrease in stress shielding and bone loss. Fouad [7] developed a finite element analysis model and compared stresses at a stiffness-graded (SG) femur head with those at femur heads fabricated from traditional stainless steel, titanium alloy, and cobalt chromium alloy. The results indicated that the contact stresses in hip-joint replacement that utilized SG were significantly lower than those with traditional materials due to absorption strain energy in a hip joint.

In the present study, the aforementioned results were used as a basis for experimentally characterizing the stiffness of materials used for body implants. It is necessary for materials used in bone replacements to possess bioactivity, biocompatibility, safety, and optimum mechanical properties [8]. Titania (TiO_2) is a biocompatible and bioactive material with good mechanical properties. Additionally, titania is irresolvable and stable in body fluids. Hence, titania is considered as an important material for bone implants [9]. However, it is necessary

to optimize and adapt the mechanical properties of titania to match the mechanical properties of bones. Specifically, it is necessary to match the stiffness of bones and titania to reduce stress shielding and bone resorption. In this respect, recent studies indicated that mechanical and physical properties, such as the strength, stiffness, and density of materials, can be optimized by designing and producing lattice structures [10]. Additionally, this approach allows the growth of new cells and tissues inside the lattice structure [11].

Additive manufacturing (AM) is a recently developed technology that allows the production of complex lattice structures with desired materials. This method is employed to obtain arbitrarily shaped parts with accurate dimensions by using computer-aided design (CAD) and computer-aided manufacturing (CAM) [12-14].

Several AM techniques have been introduced to produce porous ceramics, polymers, and metallic structures from their respective powders [15-17]. Material extrusion, selective laser sintering (SLS) and binder jetting methods all have the capability to build porous ceramics structures [18]. Material extrusion corresponds to one of the aforementioned methods and is classified as corresponding to the multi-step group by ISO/ASTM. In this method, a selected material is extruded through a nozzle and dispensed layer-by-layer on a fixed work plate to form the final shape [19]. There are several types of material extrusion methods. Guo and Leu [20] categorized material extrusion processes for filament/paste materials into three types, namely fused deposition modelling (FDM), robocasting, and freeze-form extrusion fabrication (FEF). In FDM, typical thermoplastic and wax materials are prepared by melting a filament in a nozzle, and the final product is solidified via cooling. In the other two methods (robocasting and FEF), a ceramic paste is extruded from the nozzle on a work plate. Solidification in FEF is performed by freezing the final product. Other types of material extrusion processes include multiphase jet solidification and extrusion-free forming (EFF).

Grida and Evans [21] produced zirconia (ZrO_2) based ceramics using a wax-based EFF method with various nozzle diameters. The results revealed that nozzles with a diameter smaller than 100 μm were problematic because fibers solidified prior to folding and shaping the final product. Products fabricated from nano-materials possess unique characteristics, and thus it is possible to apply the aforementioned technology in various manufacturing and design processes.

With respect to material extrusion of TiO_2, there is a paucity of studies characterizing the geometrical features (i.e., scaffold and solid structures) and their impact on the mechanical properties. Thus, the objective of the present study involves characterizing the stiffness of three-dimensional (3D) printed solid and scaffold samples fabricated from TiO_2 via extrusion. This investigation constitutes the first stage of a research project that focuses on optimizing the mechanical properties of biocompatible materials for use in bone implants. The Young's modulus of TiO_2 exceeds that of bones. Hence, the aim of the present study involves reducing the stiffness of TiO_2 samples using scaffold structures. The stiffness of the fabricated samples was measured via compression tests. The results indicated a lower stiffness for the scaffold structure when compared to that of the solid structure.

1 Materials and method

The first step involved manufacturing the scaffold and solid structures. Subsequently, the stiffness, shrinkage, grain size, and effects of the sintering temperature were compared between the two structures. Finally, the energy and particle distributions of various compositions were evaluated. The details are discussed below.

1.1 Paste preparation and specimen manufacturing

A commercially available 30 nm titanium oxide powder (rutile, high purity 99.9%, US Research Nanomaterials Inc.) was used as a base material. Bentonite powder (Quest White 3411-01) and normal water were used as a binder and solvent, respectively. In order to obtain a homogeneous mixture with sufficient density, bentonite powder was gradually added to a mixture of titanium oxide powder and water. Table 1 shows the composition of the paste and its weight percentage (wt. %).

Table 1: Composition of the experimental material

Material	wt. %
Base material (TiO_2 powder 30 nm rutile, 99.9%)	65
Solvent (normal water)	33
Binder (bentonite powder-quest white 3411-01)	2

The paste preparation process was done at room temperature. Viscosity of the paste was measured after 4 h of paste preparation. Figure 1 shows the viscosity-shear rate diagram measured using a TA Instruments AR-G2 rotational rheometer at room temperature. The paste was kept at room temperature in the laboratory and printed after 8 h.

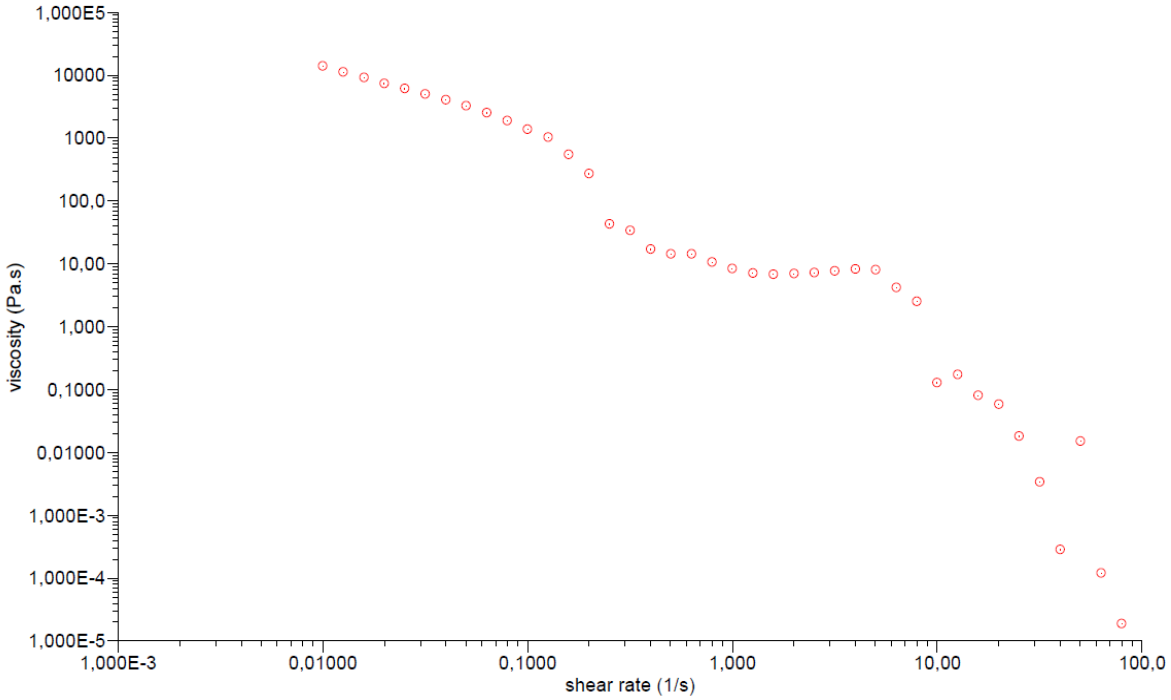

Figure 1. Viscosity-shear rate diagram of the paste.

The technical parameters of the extruder machine used to manufacture the samples were as follows: pressure behind the paste cylinder: 3–5 bars, nozzle diameter: 2 mm, and speed of extrusion: 30 mm/s. All manufacturing was done at room temperature. For all specimens, a CAD/CAM model was prepared first using the commercial software SolidWorks (see Figure 2), and the geometry was then sent to a universal extruder machine. As recommended in ASTM D695 [22], both solid and scaffold samples used for compression tests had a cylindrical shape of height H = 60 mm and diameter D = 30 mm. All specimens were printed with a layer thickness of 2 mm (see Figure 2D), equal to the nozzle diameter.

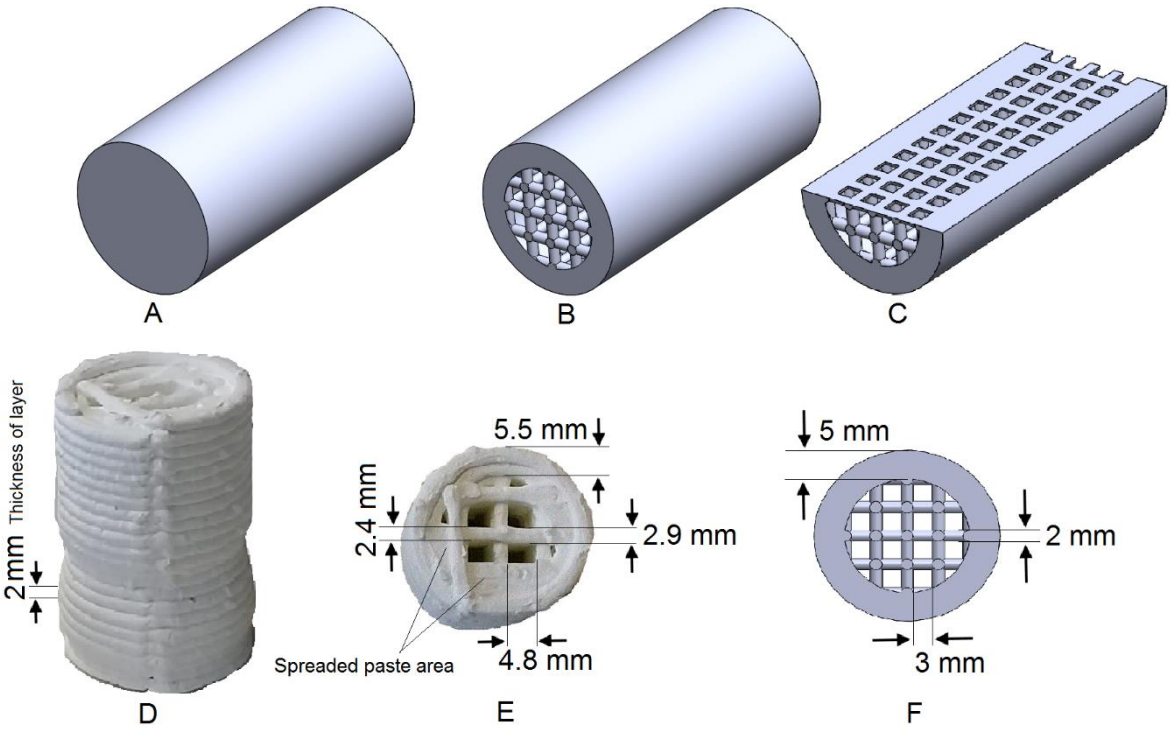

Figure 2. Geometrical dimensions of computational models and printed samples. A) Solid structure; B) scaffold structure; C) cross section of scaffold structure; D) printed scaffold structure; E) top view of printed scaffold structure; and F) top view of modeled scaffold structure.

The scaffold structure considered in this study had a geometry similar to bone, where a porous core is surrounded by a solid exterior (see CAD models in Figure 2B, C and F). The solid outer shell had a thickness of 5 mm and served as a support for the porous core. The dimensions of the porous core were selected to be at the limits of the extruder machine: the wall thickness of 2 mm was equal to the nozzle diameter and the wall spacing of 3 mm was necessary to avoid/limit the overlap of material. Based on the CAD models, the cross-sectional area of the scaffold is 29% less than that of the solid specimens. It will be shown later, in Section 3.1, that the manufactured samples after sintering also show a very similar difference in cross-sectional area (27%).

The dimensions of the printed scaffold samples were different from those of the CAD model. The wall thickness of the porous core varied between 2.4 mm and 2.9 mm and the thickness of the exterior wall was 5.5 mm instead of 5.0 mm (compare Figure 2E and F). These geometrical variations are believed to be due to changes in the extrusion pressure, and more details are given in Section 1.3.

1.2 Sintering

Sintering is a heat-treatment process that reduces porosity and increases the mechanical strength of materials at temperatures below their melting point**.** The sintering temperature is an important parameter that affects porosity, mechanical properties, and densification of sintered ceramics [8]. Specifically, 3D printed ceramic structures were consolidated via heat treatment at different sintering temperatures. The properties of titanium-dioxide and sintering conditions affect grain growth and orientation, microstructure, and mechanical and surface properties of 3D structures [23]. In order to harden the specimens, three pairs of solid and scaffold samples were sintered in a furnace at 1200 °C, 1250 °C, and 1300 °C for 4 h. The heating rate used was 10 °C/min up to 1300 °C and the cooling rate was 10 °C/min. Figure 3 shows the printed samples before and after sintering and Figure 4 illustrates the time-temperature profile of the sintering process.

Figure 3. Green body and sintered photographs of A) solid B) scaffold structures.

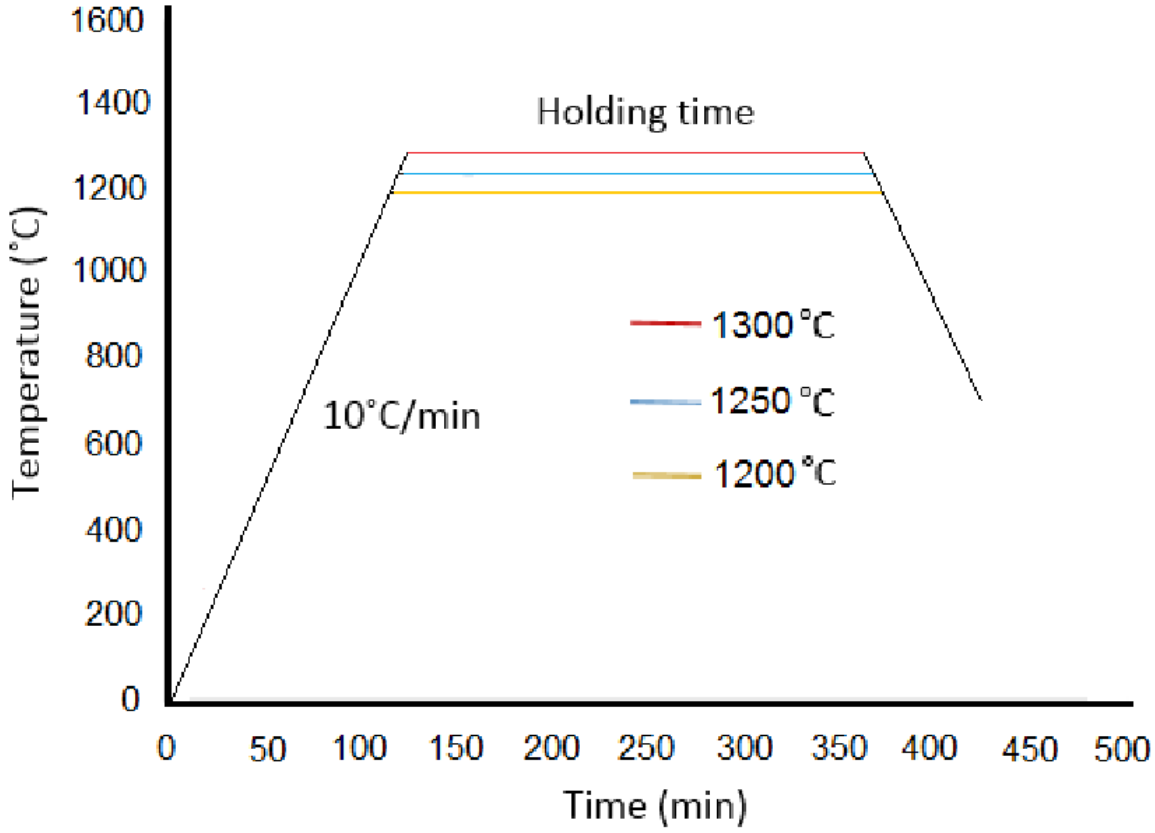

Figure 4. The time-temperature profile of furnace sintering.

1.3 Mechanical tests

The mechanical properties were determined using a universal compression test machine MTS-647 Hydraulic Wedge Grip. The samples were tested under ambient conditions and with a crosshead speed of 0.3 mm min^{-1}. The load was applied until all samples were fragmented. A clip gauge, with an initial gauge length of 12 mm was used to measure the compressive displacement. Figure 5 illustrates the compression test set up.

Figure 5. Mechanical compression test machine (MTS-647 Hydraulic Wedge Grip).

In the experiment, a few parameters were fixed, such as the CAD design, sample size, TiO_2 powder paste combination, and the operation of the mechanical testing machine. The obtained data corresponded to stiffness and microstructure SEM images. Figure 6 illustrates a parameter diagram for the experiments.

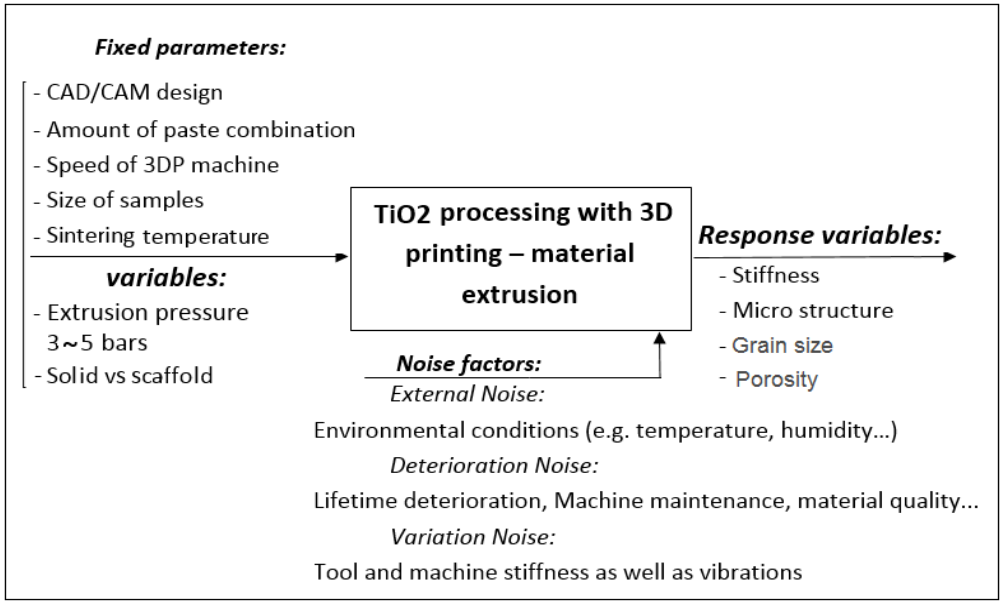

Figure 6. Parameter diagram for the experiments.

As mentioned in the parameter diagram, the extrusion pressure varied between 3 and 5 bars during printing. This was due to the existence of air bubbles inside the paste tube, and led to geometrical variations and unexpected paste spreading in some areas of lattice as shown previously in Figure 2E. These air bubbles were formed while inserting the paste into the extrusion machine tube.

2 Results and discussion

2.1 Stiffness

It is important to characterize the stiffness of structures in several engineering applications. Figure 7 shows the force–displacement curves obtained for all samples at various sintering temperatures. The results of the stiffness were analyzed at the first fracture point. Evidently, a reduction in the area of the scaffold structure decreased the allowable compressible stress when compared with that of the solid structure. There was a clear difference in energy

absorption (i.e., the area under the curve) between the scaffold and solid structures at a sintering temperature of 1200 °C, see Figure 7A. This indicated a significant decrease in the stiffness of the scaffold structure and an increase in elasticity. However, as shown in Figure 7B and C, an increase in the sintering temperature significantly improved the mechanical properties. This implied that the strength of the scaffold structure increased rapidly when the sintering temperature increased.

The stiffness of each specimen is summarized in Table 2. Clearly, scaffold samples have a lower stiffness than solid specimens: the reduction in stiffness varies from 50% to 27% when the sintering temperature is increased from 1200 °C to 1300 °C. The cross-sectional area of scaffolds is 27% smaller than that of solid samples (see Figure 8); hence, the reduction in stiffness at 1300 °C is linearly proportional to the reduction in cross-sectional area. The greater reduction in stiffness observed at lower sintering temperatures are likely to be caused by geometrical imperfections in the manufacturing process.

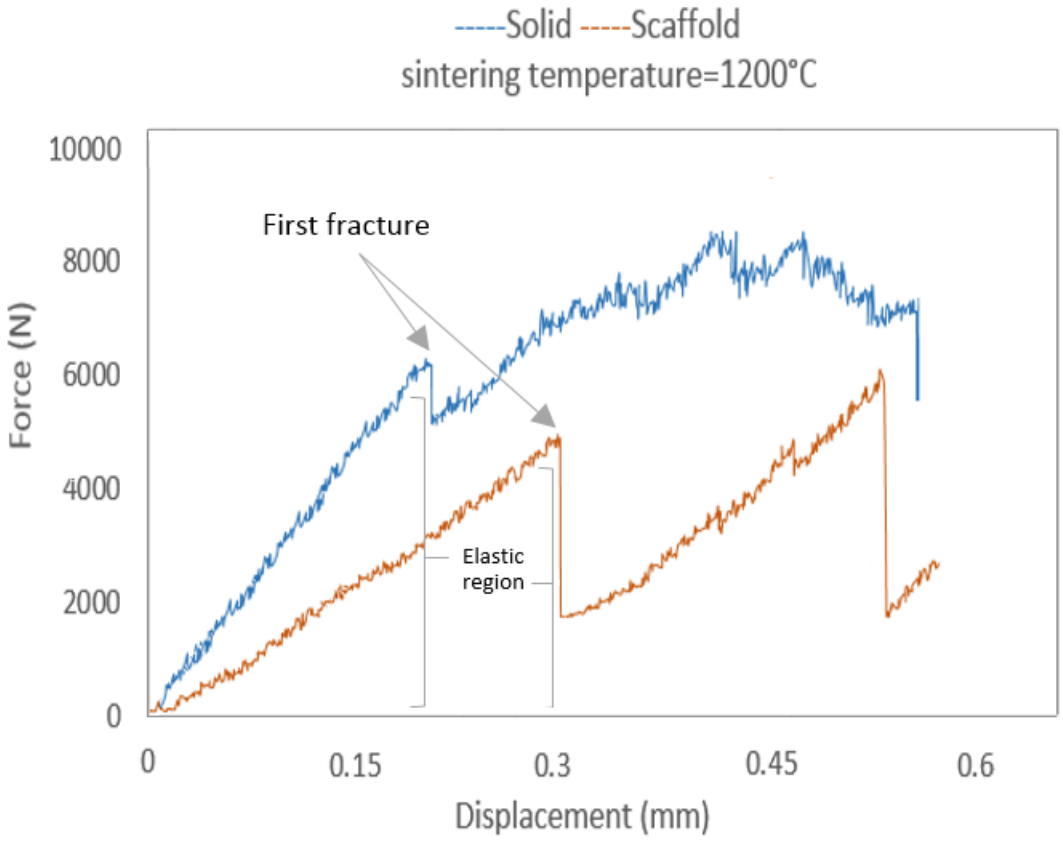
-----Solid -----Scaffold
sintering temperature=1200°C
10000
8000
6000
4000
2000
0
Force (N)
First fracture
Elastic region
0
0.15
0.3
0.45
0.6
Displacement (mm)

A

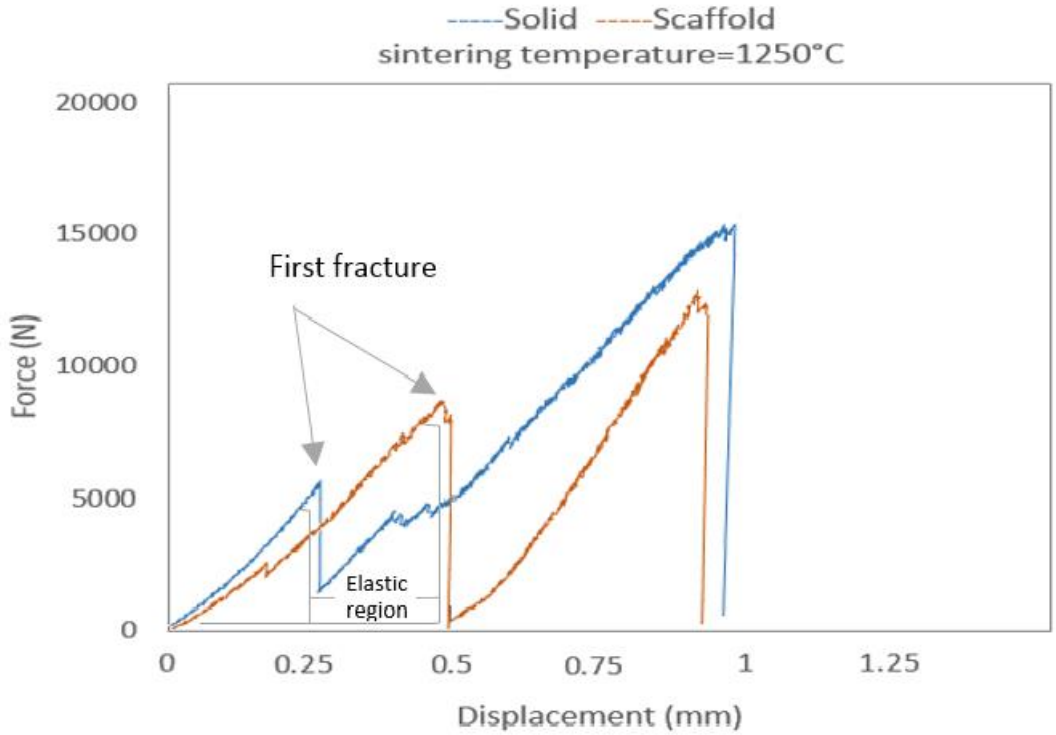
-----Solid -----Scaffold
sintering temperature=1250°C
20000
15000
10000
5000
0
Force (N)
First fracture
Elastic region
0
0.25
0.5
0.75
1
1.25
Displacement (mm)

B

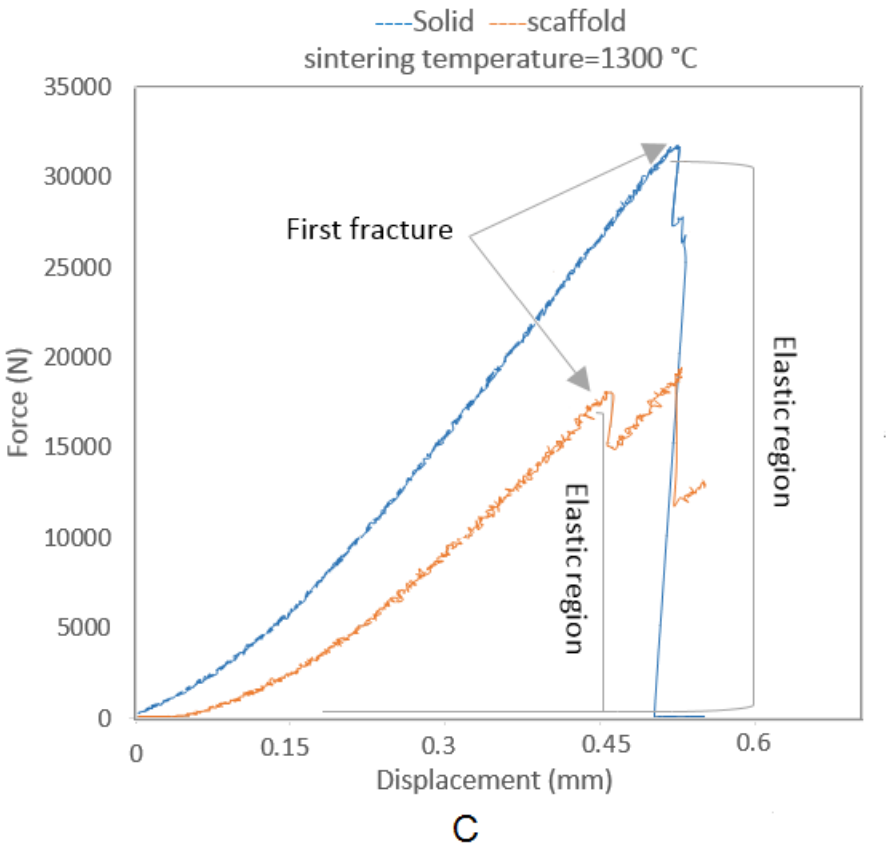

Figure 7. Compressive force-displacement responses for solid and scaffold samples fabricated via 3D printing with sintering temperatures of A) 1200 °C, B) 1250 °C, and C) 1300 °C.

Table 2: Stiffness of solid and scaffold samples for different sintering temperatures.

Sintering temp. (°C)	Solid structure stiffness (N/mm)	Scaffold structure stiffness (N/mm)
1200	3×10^4	1.5×10^4
1250	2.4×10^4	1.6×10^4
1300	5.8×10^4	4.2×10^4

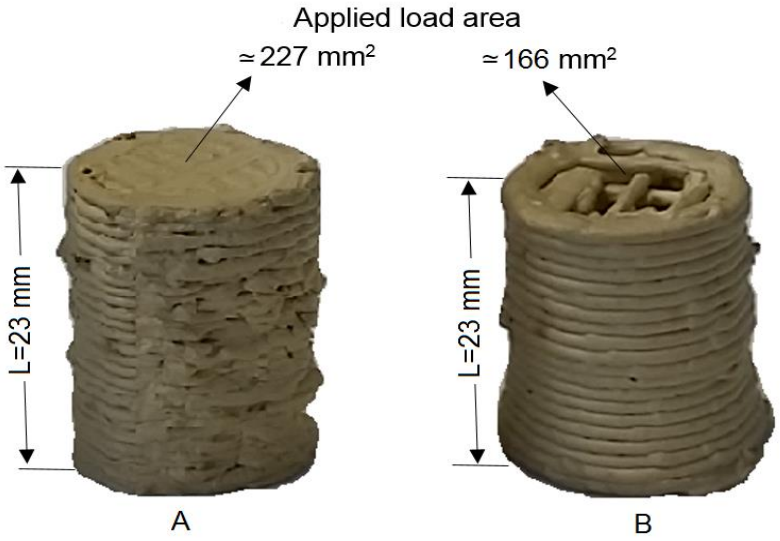

Figure 8. Length and cross-sectional area of A) solid and B) scaffold structures.

Using the stiffness values in Table 2 and the cross-sectional areas in Figure 8, it is possible to calculate the elastic modulus of TiO_2 for the samples manufactured. The elastic modulus of TiO_2 for our samples varies between 2.08-5.90 GPa, see Table 3. Interestingly, this is close to the elastic modulus of high density cancellous bone, which varies from 0.8 to 1.5 GPa [24]. However, the printed material is significantly more compliant than that obtained with conventional manufacturing methods which give an elastic modulus between 230-280 GPa [24], We anticipate that the binder and its particles are responsible for this discrepancy.

Table 3: Elastic modulus of TiO_2 obtained from tests on solid and scaffold structures.

Sintering temp. (°C)	Elastic modulus of solid structure (GPa)	Elastic modulus of scaffold structure(GPa)
1200	3.04	2.08
1250	2.43	2.22
1300	5.90	5.81

2.2 Shrinkage

Figure 9 shows the shrinkage of the scaffold structure after being sintered at 1200 ˚C. Intense shrinkage happened in all dimensions x, y and z.

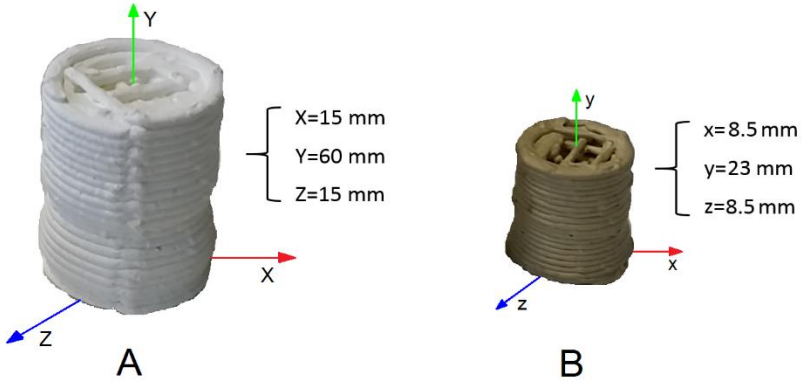

Figure 9. A) Green body scaffold structure and B) scaffold structure shrunk after sintering at 1200 ˚C.

The dimensions before and after sintering are summarized in Table 4. For each direction, a measure of the average shrinkage (AS) for both solid and scaffold structures is also included. The results reveal that the maximum shrinkage (57.5%) has happened in the y-direction (perpendicular to the work plate). Comparing solid and scaffold structures shows that the shrinkage of solid structures is less than that of scaffolds in all directions. Different sintering temperatures did not show considerable shrinkage alteration.

Table 4: Dimensions of printed samples before and after sintering, and average shrinkage at 1200 ˚C

Green body solid & scaffold structure dimensions X, Y, Z (mm)	Sintered solid structure dimensions x,y,z (mm)	Sintered scaffold structure dimensions x,y,z (mm)	Average shrinkage (AS) for both structures (%)
X=15	x=9	x=8.5	$AS_X = 41.6$
Y=60	y=28	y=23	$AS_Y = 57.5$
Z=15	z=9	z=8.5	$AS_Z = 41.6$

2.3 Morphology

The morphology of the samples was characterized by scanning electron microscopy (SEM). The microstructures were observed using a desktop micro-CT scanner, and images are shown in Figure 10 for the three sintering temperatures considered.

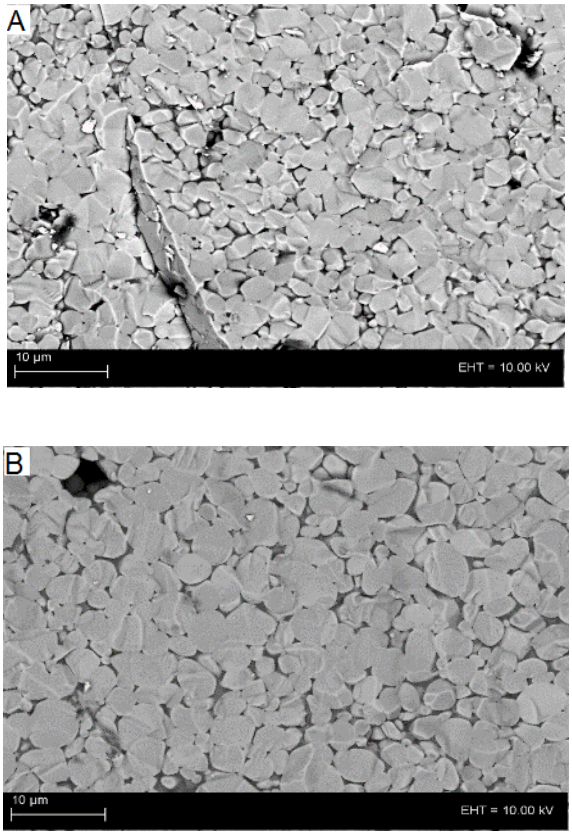

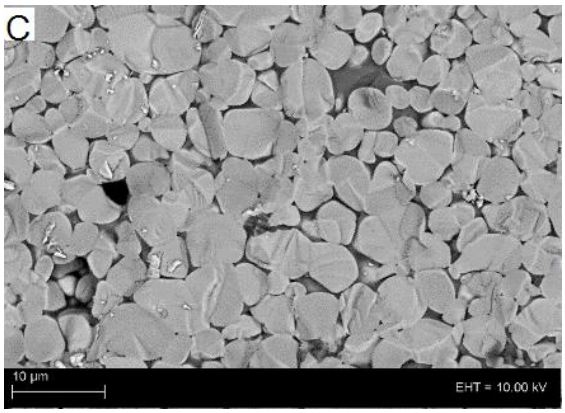

Figure 10. SEM images of the samples in which the scale bar represents 10 µm. Images are shown for a sintering temperature of A) 1200 °C; B) 1250 °C and C) 1300 °C.

The results indicate that the samples sintered at a lower temperature had nanosize grains that were randomly distributed and irregularly oriented. However, a comparison of the grain sizes at sintering temperatures of 1200 °C, 1250 °C, and 1300 °C revealed that the grain size increased significantly at 1,300 °C. Figure 11 shows the average grain size at the three sintering temperatures considered. The histogram shows that the average grain size at 1300 °C is approximately twice that at 1200 °C.

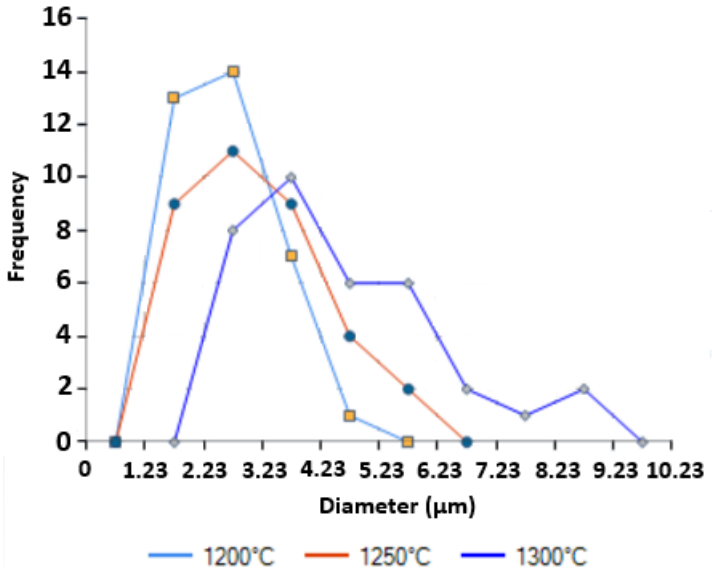

Figure 11. Histograms of grain sizes for samples sintered at different temperatures.

The average grain sizes correspond to 2.52 µm, 3.15 µm, and 4.67 µm at 1200 °C, 1250 °C, and 1300 °C, respectively.

The CT images shown in Figure 10 were also used to analyze the porosity of the samples. The analysis was done using the software ImageJ and with images considering an area of about 240 μm^2. The results, shown in Figure 12, show that increasing the sintering temperature from 1200 °C to 1300 °C decreases the porosity from 10% to 8%. Repeating this analysis with other images of the same samples showed that the error on porosity is of the order of 1-2%.

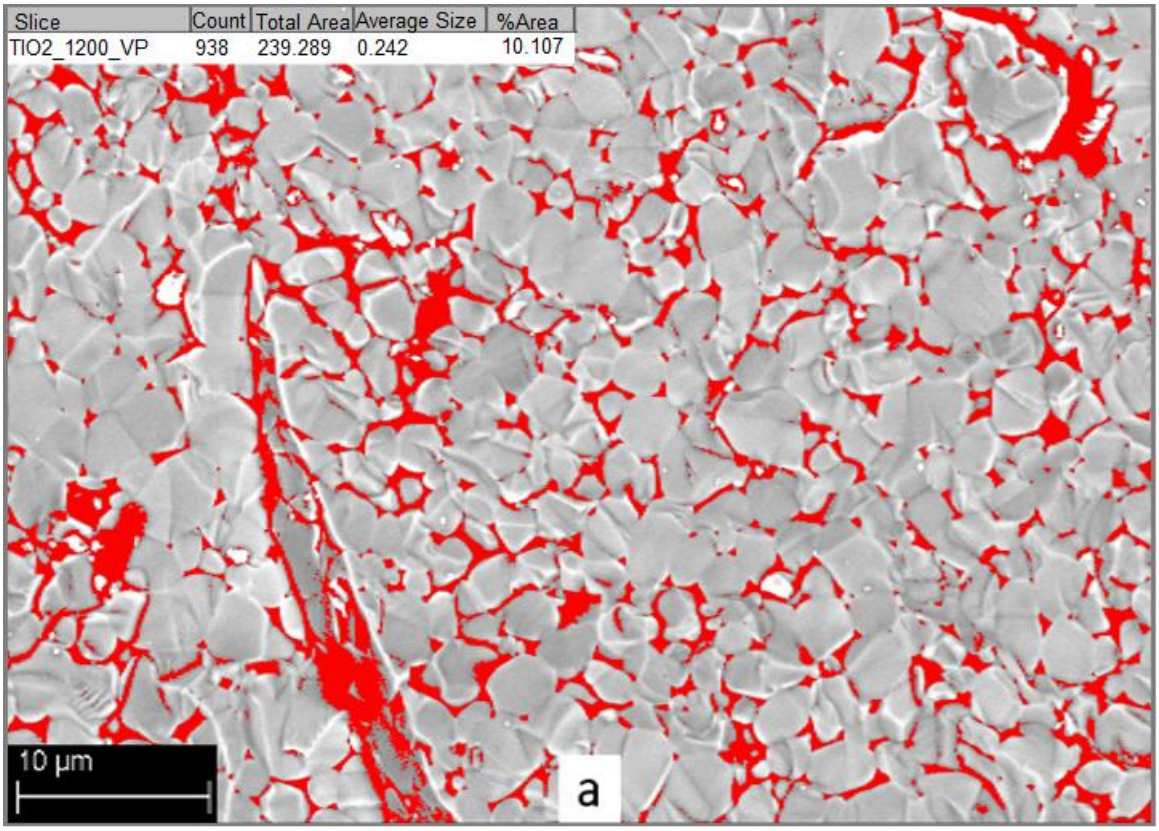

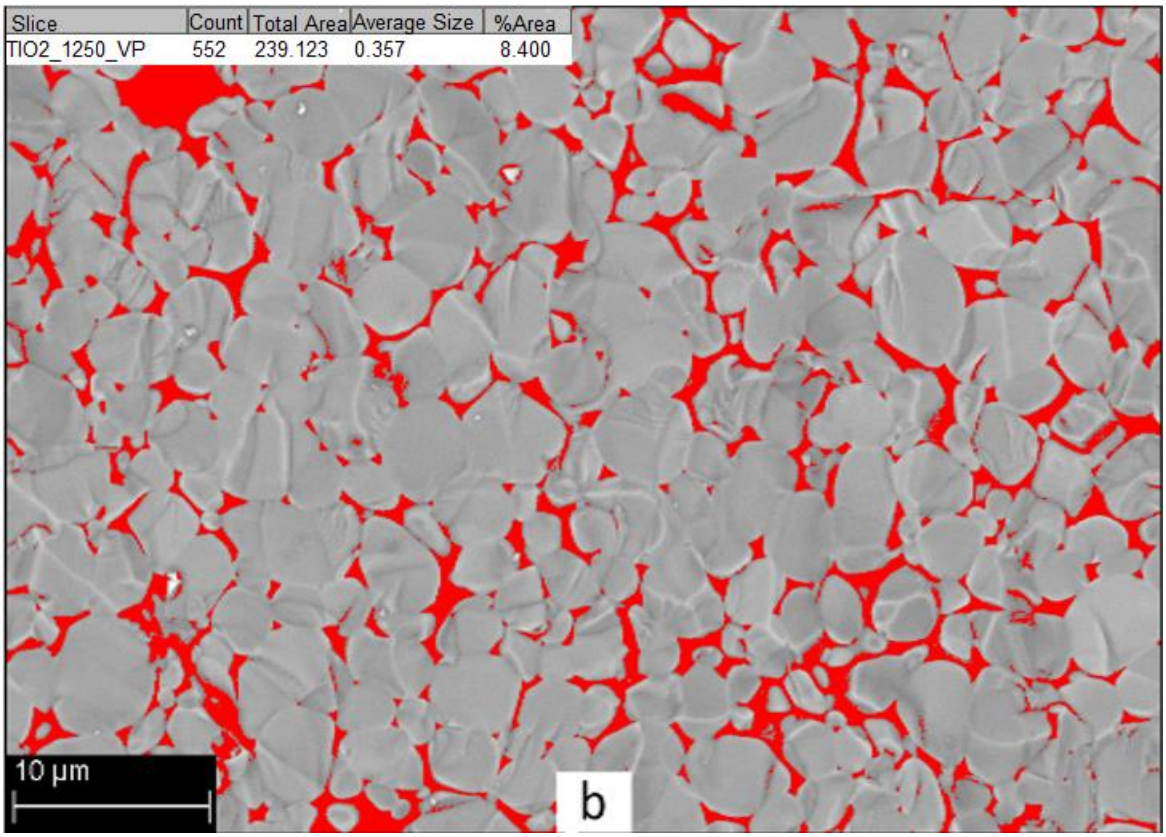
Slice Count Total Area Average Size %Area
TIO2_1250_VP 552 239.123 0.357 8.400
10 µm
b

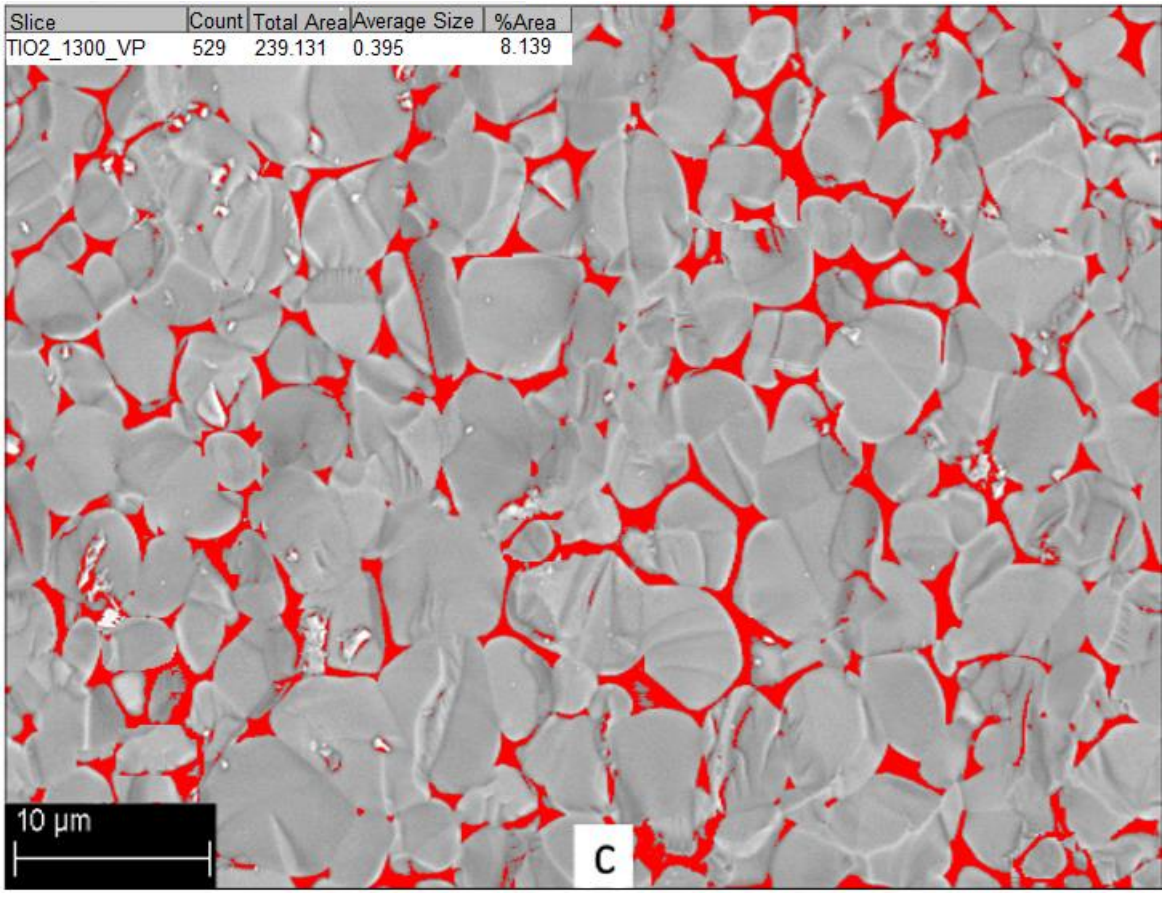
Slice Count Total Area Average Size %Area
TIO2_1300_VP 529 239.131 0.395 8.139
10 µm
c

Figure 12. Porosity for samples sintered at A) 1200 °C, porosity of 10.1%; B) 1250 °C, porosity of 8.4%; and C) 1300 °C, porosity of 8.1%. In all cases, the area considered is about 240 μm^2

Finally, the energy and particle distribution for various materials were evaluated and the results are shown in Figure 13 for the three sintering temperature considered. Although material energy remained constant when the sintering temperature increased, the particle distribution changed significantly. Additionally, the results indicated that Ti and O exhibited the highest and lowest energy contents, respectively.

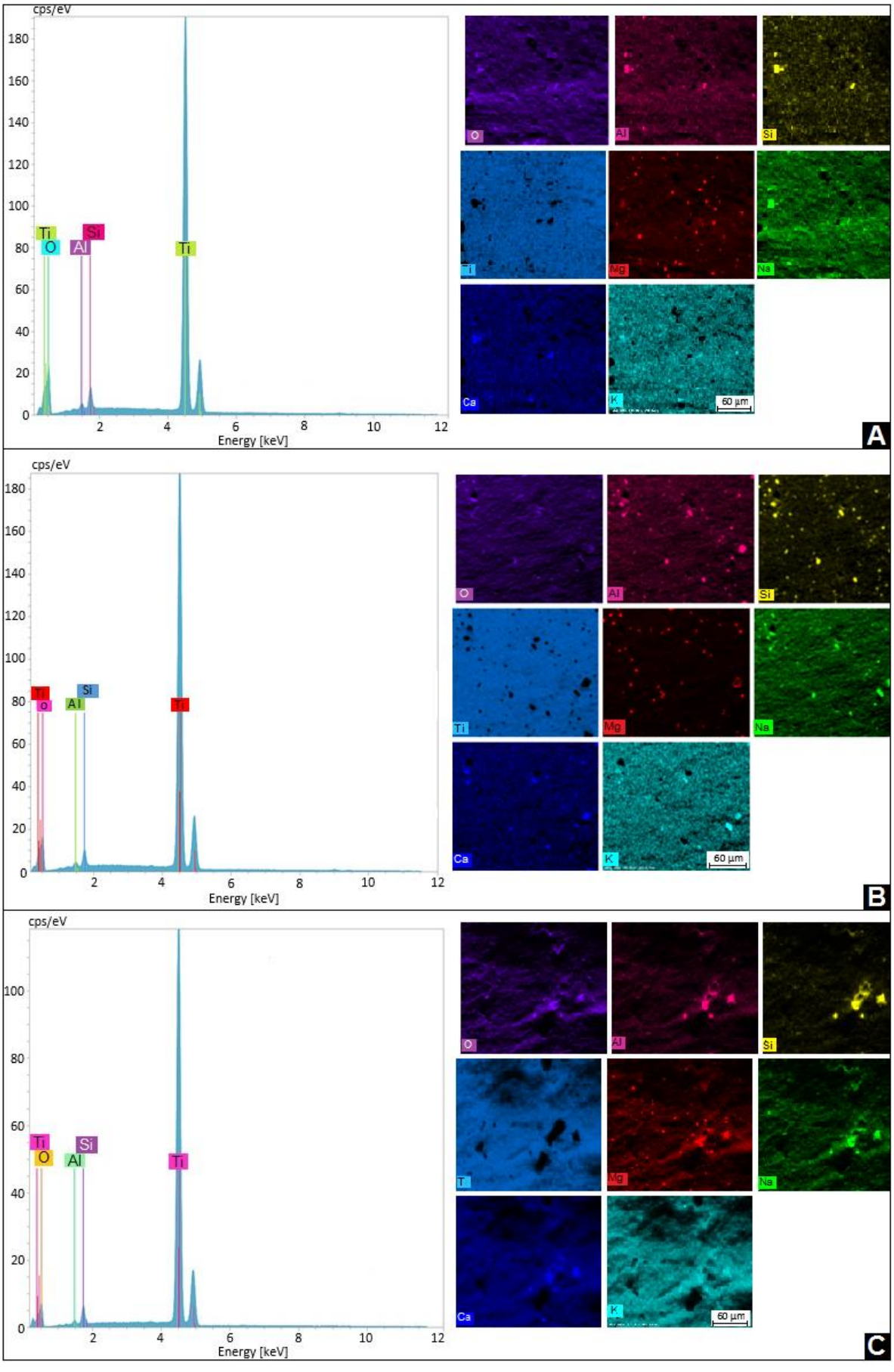
cps/eV
Energy [keV]
Ti
O
Al
Si
Ti
O
Al
Si
Ca
K
60 µm
A
cps/eV
Energy [keV]
Ti
O
Al
Si
Ti
O
Al
Si
Ca
K
60 µm
B
cps/eV
Energy [keV]
Ti
O
Al
Si
Ti
O
Al
Si
Ca
K
60 µm
C

Figure 13. Energy and particle distributions for samples sintered at A) 1200 °C, B) 1250 °C and C) 1300 °C.

3 Conclusion

Scaffold structures of a bioactive material can significantly reduce bone absorption and stress shielding when compared with solid structure implants. Furthermore, scaffold structure implants allow living cells to grow inside a porous area. Thus, the present study involved using an experimental approach to measure and compare the stiffness of 3D printed solid and scaffold TiO_2 structures produced for bone implants. The results are as follows:

1. The stiffness of the scaffold structures was 27% to 50% lower than that of the solid structures. This reduction is in line with the fact that the cross-sectional area of scaffolds was about 27% smaller than that of the solid samples.

2. The elastic modulus of the printed TiO_2 material varied between 2.08-5.90 GPa. While this value is significantly less than the modulus obtained from conventional manufacturing methods (230-280 GPa) it has the advantage to be relatively close to the elastic modulus of bone (0.8-1.5 GPa for high density cancellous bone).

3. Sintering caused shrinkage in all directions. The maximum shrinkage was 57.5% in the direction perpendicular to the work plate. Shrinkage was fairly constant for all three sintering temperatures considered.

4. The grain size increased significantly with increasing sintering temperature. The average grain size at 1300 °C was approximately twice that at 1200 °C.

5. The porosity decreased with increasing sintering temperature. The porosity at 1300 °C was 20% lower than that at 1200 °C.

6. Although an increase in the sintering temperature did not change the material energy, the particle distribution exhibited significant changes.

In this study, variations in the extrusion process lead to differences in the geometrical dimensions of the samples. A future study will investigate if this problem can be alleviated using other AM technologies, such as binder jetting methods.

References

[1] J.A. Disegi, L. Eschbach, Stainless steel in bone surgery, Injury. 31 (2000). doi:10.1016/S0020-1383(00)80015-7.

[2] H.J. Rack, J.I. Qazi, Titanium alloys for biomedical applications, Mater. Sci. Eng. C. 26 (2006) 1269–1277. doi:10.1016/j.msec.2005.08.032.

[3] O.E.M. Pohler, Unalloyed titanium for implants in bone surgery, Injury. 31 (2000). doi:10.1016/S0020-1383(00)80016-9.

[4] C. Piao, D. Wu, M. Luo, H. Ma, Stress shielding effects of two prosthetic groups after total hip joint simulation replacement, J. Orthop. Surg. Res. 9 (2014) 71. doi:10.1186/s13018-014-0071-x.

[5] M.I.Z. Ridzwan, S. Shuib, A.Y. Hassan, A.A. Shokri, M.N. Mohammad Ibrahim, Problem of stress shielding and improvement to the hip implant designs: A review, J. Med. Sci. 7 (2007) 460–467. doi:10.3923/jms.2007.460.467.

[6] R. Huiskes, H. Weinans, B. van Rietbergen, The relationship between stress shielding and bone resorption around total hip stems and the effects of flexible materials., Clin. Orthop. Relat. Res. (1992) 124–134.

[7] H. Fouad, In vitro evaluation of Stiffness Graded artificial hip joint femur head in terms of joint stresses distributions and dimensions: Finite element study, J. Mater. Sci. Mater. Med. 22 (2011) 1589–1598. doi:10.1007/s10856-011-4319-2.

[8] I. Pires, B. Gouveia, J. Rodrigues, R. Fonte, Characterization of sintered hydroxyapatite samples produced by 3D printing, Rapid Prototyp. J. 20 (2014) 413–421. doi:10.1108/RPJ-

05-2012-0050.

[9] 2 Michiko Sato, 1 Arash Aslani, 2 Marisa A. Sambito, 2 Nader M. Kalkhoran, 1 Thomas J. Webster Elliott B. Slamovich, Nanocrystalline hydroxyapatite/titania coatings on titanium improves osteoblast adhesion, Wiley Intersci. (2007).

[10] D. Rosen, S. Johnston, M. Reed, Design of General Lattice Structures for Lightweight and Compliance Applications, Rapid Manuf. Conf. (2006) 1–14. http://smartech.gatech.edu/handle/1853/33037.

[11] D.W. Hutmacher, Scaffolds in tissue engineering bone and cartilage., Biomaterials. 21 (2000) 2529–2543. doi:10.1016/S0142-9612(00)00121-6.

[12] K. V. Wong, A. Hernandez, A Review of Additive Manufacturing, ISRN Mech. Eng. 2012 (2012) 1–10. doi:10.5402/2012/208760.

[13] I. Gibson, D.W. Rosen, B. Stucker, Additive manufacturing technologies: Rapid prototyping to direct digital manufacturing, 2010. doi:10.1007/978-1-4419-1120-9.

[14] a. . Cooper, S. Kang, J.. Kietzman, F.. Prinz, J.. Lombardi, L.. Weiss, Automated fabrication of complex molded parts using Mold Shape Deposition Manufacturing, Mater. Des. 20 (1999) 83–89. doi:10.1016/S0261-3069(99)00013-8.

[15] J. An, J.E.M. Teoh, R. Suntornnond, C.K. Chua, Design and 3D Printing of Scaffolds and Tissues, Engineering. 1 (2015) 261–268. doi:10.15302/J-ENG-2015061.

[16] M. Castilho, M. Dias, U. Gbureck, Fabrication of computationally designed scaffolds by low temperature 3D printing, Biofabrication. 66 (2013) 911–917. doi:10.1088/1758-5082/5/3/035012.

[17] A. Farzadi, V. Waran, M. Solati-Hashjin, Z.A.A. Rahman, M. Asadi, N.A.A. Osman, Effect of layer printing delay on mechanical properties and dimensional accuracy of 3D printed porous prototypes in bone tissue engineering, Ceram. Int. 41 (2015) 8320–8330. doi:10.1016/j.ceramint.2015.03.004.

[18] Seitz, Hermann, et al. "Three-dimensional printing of porous ceramic scaffolds for bone tissue engineering." Journal of Biomedical Materials Research Part B: Applied Biomaterials 74.2 (2005): 782-788.

[19] J. Deckers, J. Vleugels, J.P. Kruth, Additive manufacturing of ceramics: A review, J. Ceram. Sci. Technol. 5 (2014) 245–260. doi:10.4416/JCST2014-00032.

[20] N. Guo, M.C. Leu, Additive manufacturing: Technology, applications and research needs, Front. Mech. Eng. 8 (2013) 215–243. doi:10.1007/s11465-013-0248-8.

[21] I. Grida, J.R.G. Evans, Extrusion freeforming of ceramics through fine nozzles, J. Eur. Ceram. Soc. 23 (2003) 629–635. doi:10.1016/S0955-2219(02)00163-2.

[22] ASTM D695-15, Standard Test Method for Compressive Properties of Rigid Plastics, ASTM

International, West Conshohocken, PA, 2015.

[23] S. Chao, V. Petrovsky, F. Dogan, Effects of sintering temperature on the microstructure and dielectric properties of titanium dioxide ceramics, J. Mater. Sci. 45 (2010) 6685–6693.

[24] CES EduPack 2017, Granta Design Limited, Cambridge, UK, 2017.